PHYSICS OF PLASMAS 23, 113503 (2016)

Ion flow and sheath structure near positively biased electrodes

R. Hood,[1] B. Scheiner,[1] S. D. Baalrud,[1] M. M. Hopkins,[2] E. V. Barnat,[2] B. T. Yee,[2] R. L. Merlino,[1] and F. Skiff[1]
[1]*Department of Physics and Astronomy, University of Iowa, Iowa City, Iowa 52242, USA*
[2]*Sandia National Laboratories, Albuquerque, New Mexico 87185, USA*

(Received 6 September 2016; accepted 1 November 2016; published online 16 November 2016)

What effect does a dielectric material surrounding a small positively biased electrode have on the ion flow and sheath structure near the electrode? Measurements of the ion velocity distribution function and plasma potential near positively biased electrodes were made using laser-induced fluorescence and an emissive probe. The results were compared with 2D particle-in-cell simulations. Both measurements and simulations showed that when the positive electrode was surrounded by the dielectric material, ions were accelerated toward the electrode to approximately 0.5 times the ion sound speed before being deflected radially by the electron sheath potential barrier of the electrode. The axial potential profile in this case contained a virtual cathode. In comparison, when the dielectric material was removed from around the electrode, both the ion flow and virtual cathode depth near the electrode were dramatically reduced. These measurements suggest that the ion presheath from the dielectric material surrounding the electrode may enclose the electron sheath of the electrode, resulting in a virtual cathode that substantially influences the ion flow profile in the region. *Published by AIP Publishing.* [http://dx.doi.org/10.1063/1.4967870]

I. INTRODUCTION

Sheaths are regions of net space charge near the boundaries of most plasmas and maintain current balance by limiting the current of different charge species leaving the plasma. Electron sheaths form near surfaces biased above the plasma potential and have a small presheath potential drop compared to an ion presheath, nominally a factor of the ion to electron temperature ratio (T_i/T_e) smaller.[1,2] Since the electron presheath potential drop is very small for a typical low-temperature plasma, where $T_e \gg T_i$, it is generally assumed that ions near a positive electrode have no flow and thus obey a Boltzmann density relation.[2,3] However, particle-in-cell (PIC) simulations in Ref. 3 have shown that this assumption may not be valid when a dielectric surface is nearby. In this paper, we verify these results experimentally and with another simulation. The question of the conditions under which virtual cathodes can form and the associated ion flow is also addressed. We find that the ion presheath associated with the dielectric alters the sheath structure in front of the positive electrode, causing the formation of a virtual cathode and an associated ion flow. These results may have implications for diagnostics and other applications where positively biased electrodes are used near dielectric surfaces, such as Langmuir probes.

Small positive electrodes occur most commonly in plasma devices when Langmuir probes are swept to electron saturation but are also found in fusion research devices to control the scrape-off layer[4,5] and in laboratory plasmas for electron temperature control.[6] Generally, dielectric material separates an electrode from the rest of the chamber. However, the dielectric can be large or small compared to the electrode and may surround or be isolated from the plasma facing surface, depending on the application. It is important to understand the effect of the dielectric near these objects since the potential dips and large ion flows generated can have significant effects on the system by altering the density profile and electron current to the boundary. In Ref. 7, the presence of a virtual cathode was shown to flatten the I-V trace of a Langmuir probe, resulting in overestimation of T_e by up to 30%. In Ref. 8, virtual cathodes are suggested to alter the sheath admittance near a positively biased planar probe, which is relevant to plasma processing and sheath modeling.

The sheath structure has been studied near positive electrodes in a number of papers.[1,3,7,9–16] Virtual cathodes, which are dips in the potential profile near the electrode, were observed in some cases,[7,9–12] but not in others.[1,3,13–16] A significant open question remains to understand the conditions under which these virtual cathodes form, and the associated ion flow response. The possible influence of ion pumping of a virtual cathode or the presence of a stable monotonic electron sheath is also an important question for understanding the sheath structure near strongly emitting boundaries.[17] The present measurements, which highlight the role of surrounding dielectrics, may influence this topic. Ref. 9 suggests that ion pumping is required for a virtual cathode to be stable at steady-state, and that this can be achieved through a saddle-shaped potential structure that provides a path for ion loss to a nearby dielectric. Here, we report time-averaged potential measurements that are consistent with this conclusion. Ref. 11 states that the general sheath structure near a positive boundary is dependent on the ratio of the electron to ion collection area in the system. Monotonic electron sheaths can only form when this ratio is less than $\sqrt{2.3m_e/M_i}$. Larger electrodes raise the plasma potential and form either a virtual cathode or an ion sheath depending on the electron collection area. Thus far, ion flow measurements near small positive electrodes have been limited to simulations and have not been focused on the role of the dielectric.[3]

This paper presents measurements of the ion velocity distribution function (IVDF) and plasma potential from a multidipole experiment using argon for two electrodes with contrasting dielectric geometries. In addition, corresponding measurements from a PIC simulation using helium with similar electrodes and plasma conditions are also presented. For one electrode, the dielectric was minimized and isolated from the positive conducting surface, hereafter referred to as the "free electrode". For the other electrode, the conducting surface was embedded in a large disc of dielectric, hereafter referred to as the "embedded electrode". The experimental IVDF and plasma potential were measured in 2D using laser-induced fluorescence (LIF) and an emissive probe diagnostic, respectively. In both the experiment and simulation, the electrode was chosen to be small enough to meet the monotonic electron sheath requirement from Ref. 11. However, we found that a virtual cathode can form in this situation if the electrode is embedded in a dielectric layer.

The plasma potential and ion flow near the electrode were observed to change significantly between the two electrodes. In both cases, ions were observed to flow toward the electrode. However, the velocity was about 10 times greater near the embedded electrode compared to the free electrode, reaching approximately 0.5 times the ion sound speed before the ions were deflected by the electron sheath potential. Similarly, a virtual cathode was observed in both cases but was roughly 3 times deeper near the embedded electrode. We consider the flow and potential dip near the free electrode to be insignificant, since their magnitudes were very weak compared to the case of the embedded electrode (and were near the experimental noise level). The results from the PIC simulation show a reasonable qualitative agreement with the experiment and also provide additional details of the 2D IVDFs that were not accessible experimentally.

This paper is organized as follows: Sec. II gives a description of the experimental setup and diagnostic systems, Sec. III gives a description of the PIC simulation, Sec. IV presents the results of the experiment and simulation with discussion, and Sec. V provides a summary.

II. EXPERIMENT DESCRIPTION

Argon plasma was produced in a 73 cm long $\times$ 49 cm diameter multidipole chamber through impact ionization by primary electrons emitted from a hot cathode biased at -115 V with respect to the grounded chamber walls. The cathode consisted of a resistive graphite bar used to heat a pocket of lanthanum-hexaboride (LaB6) powder. Emission current from the plasma source was regulated at 35 ± 1 mA. The multidipole confinement consisted of a magnet cage with 16 rows of magnets with alternating poles covering all inside walls of the chamber and was electrically connected to the grounded chamber wall. The maximum field strength was 1000 G near the surface of the magnets and less than 2 G in the measurement region. Measurements were made above the positively biased electrode, which was placed on a translatable shaft inserted from the bottom of the chamber. Neutral pressure was regulated using a mass flow controller set to 10.00 sccm of argon resulting in a constant pressure of 4.0×10^{-4} Torr, while the system base pressure was less than 10^{-6} Torr. A schematic of the device is shown in Fig. 1(a).

A spatially resolved LIF diagnostic was used to measure the IVDF with axial and radial velocity resolution above each electrode using multi-channel photomultiplier tubes (PMTs). Radial spatial resolution was provided by imaging the fluorescence collection volume onto each linear array of 16 PMT channels, while axial spatial resolution was provided by moving the electrode vertically as shown schematically in Fig. 1(b). This system allowed the fluorescence collection optics to remain stationary, which greatly simplified the design. The common three level LIF scheme for ArII was utilized,[18] where ions are excited from a metastable energy level by laser radiation near 611.66 nm and decay, emitting a fluorescence photon at 461.1 nm. This was accomplished using emission from a tunable dye laser (Sirah Matisse-DS), which was sent to the chamber using a multimode fiber optic cable. The beam was injected either axially or radially into the chamber depending on which velocity component was being measured. Since an absolute frequency reference was not available for laser calibration, the unshifted absorption line center was found by measuring axial and radial IVDFs in the bulk plasma. The resulting systematic error for velocity measurements was $\sim 3 \times 10^3$ cm s^{-1} (the random error was much smaller). The fluorescence signal was observed through a 25 cm diameter window that provided a large solid-angle view of the collection volume, which was desired to improve the signal to noise ratio. The effective depth of field for the collection volume was set by the width of the laser, which was approximately 0.9 cm. The fluorescence signal was split into two beams and each was: sent through a slit (this set the height of the collection volume), filtered using narrow bandwidth interference filters, and imaged onto 16-channel PMTs. A schematic of the optics is shown in Fig. 1(a). Here, the experiment is shown configured for radial velocity measurements with the laser propagating from left to right (laser propagation would be into the page for axial velocity measurements). Measurements of the IVDF were made in the radial and axial directions for both electrode geometries. For each electrode and velocity component, the fluorescence signal was measured for 36 s at each of the 15 axial electrode positions and 35 discrete laser wavelengths. Combined with the radial spatial resolution (using the linear array of 16 PMT channels), this provided 1D radial and axial projections of the full 3D IVDF at 240 spatial locations above each electrode.

The two electrode geometries used in the experiment are shown in Fig. 1(c). The electrode on the right had a dielectric surrounding the conducting surface (embedded electrode), whereas the one on the left had a minimal dielectric, which covered only a small portion of the bottom of the electrode near the support rod (free electrode). Each was biased to $+10$ V with respect to ground (about 5 V above the plasma potential). The top of each electrode consisted of a razor blade stack to reduce backscattered laser light. The spacing between blade edges in the stack was smaller than the electron Debye length, so the perturbation to the electric field due to surface roughness was considered to be negligible.

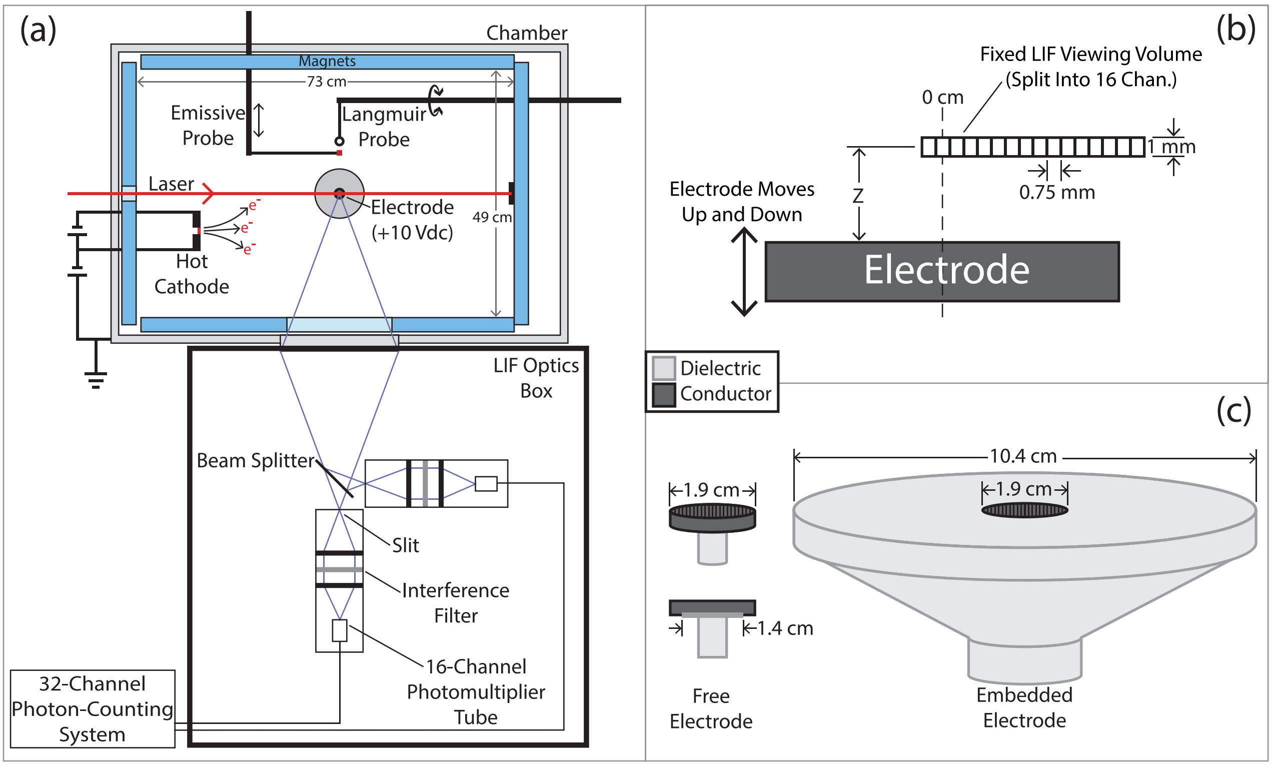

FIG. 1. Experiment schematics: (a) top view of the experimental setup (laser is shown configured for radial velocity measurements, for axial velocity measurements the laser points into the page), (b) schematic view of the LIF viewing volume above the electrode, shown at Z = 0.5 cm (channel 2 was placed at R = 0 to simplify optical alignment procedure), (c) schematic diagram of both electrode designs used in the experiment (conductor shown in dark gray, dielectric in light gray).

A 3.2 mm diameter disc-shaped Langmuir probe was used to measure electron temperature, T_e, and electron density, n_e, in the bulk plasma and an emissive probe was used to measure the plasma potential, V_p, using the floating point technique[19] in a 2D grid above each electrode. The emissive probe was constructed from the filament of a very small incandescent light bulb (probe dimensions 2 mm wide × 0.3 mm tall). Typical plasma parameters during the experiment were, $T_e = 1.3$ eV, $n_e = 7.3 \times 10^9$ cm^{-3}, and $V_p = 4.5$ V (bulk plasma values). This gives an ion sound speed, c_s, of approximately 1.8×10^5 cm s^{-1}.

III. SIMULATION DESCRIPTION

Simulations were performed using the electrostatic PIC code Aleph.[16,20] A 2D triangular mesh was used to discretize the two simulation domains shown in Fig. 2. Each domain was 15 cm × 5 cm and was bounded on three sides with a Dirichlet $V = 0$ boundary condition and one side with a Neumann $\nabla V \cdot \hat{\mathbf{n}} = 0$ boundary condition. The wall with the Neumann boundary condition was reflecting for particles. By symmetry, the simulation domain represents a physical domain of 15 cm × 10 cm. Each domain had an electrode placed perpendicular to the midpoint of the reflecting boundary. In the first case, shown in Fig. 2(a), the electrode was configured to represent the free electrode in the experiments. This model was of length 0.2 cm and biased at 25 V. A small section of the back was biased at 0 V and was meant to model the dielectric support for the electrode used in the experiment. The 0 V and 25 V regions were separated by a small gap (0.05 cm long) in which the potential at the surface was allowed to vary. A second configuration, shown in Fig. 2(b), was used to model the embedded electrode. In this case, the boundary was 0.8 cm with a small section of length 0.2 cm along the face of the electrode biased at 25 V and the rest biased at 0 V. Again, the 0 V and 25 V regions were separated by a small gap (0.2 cm long). The simulation used grounded conducting boundaries in place of the dielectric used in the experiment, since this produced the desired ion sheath without the complication of surface charging. The size of each mesh element was 0.02 cm such that the electron Debye length ($\lambda_{De} = 0.04$ cm) was resolved. The simulation domain was filled with a helium plasma generated at a rate of 10^{20} cm^{-3} s^{-1} within the volume at temperatures of 0.08 eV for ions and 4 eV for electrons, each with a macro-particle weight of 2000. The resulting bulk density was approximately $n_e = 7 \times 10^8$ cm^{-3}. Helium was used in the simulation rather than argon to reduce computation time. The time step of 5×10^{-11} s resolved the electron plasma frequency ($f_{Pe} = 24$ MHz) and ensured that the plasma particles satisfied the Courant-Friedrichs-Lewy (CFL) condition.[21] Each simulation ran for 800 000 time steps totaling 40 μs of physical time.

Since simulations were 2D, the appropriate electron temperature for calculation of the ion sound speed is the 2D electron temperature. This was calculated 1 cm above the electrode face by using only x and y velocity components, i.e., $T_e = n_e \int d^2v\, m_e(v_{r,x}^2 + v_{r,y}^2) f_e/2$, where $f_e(\mathbf{v})$ is the electron velocity distribution function, n_e is the electron density, and $v_{r,i} = (\mathbf{v} - \mathbf{V_e}) \cdot \hat{\mathbf{i}}$, where $\mathbf{V_e} = \frac{1}{n_e}\int d^2 v \mathbf{v} f_e$ is the flow

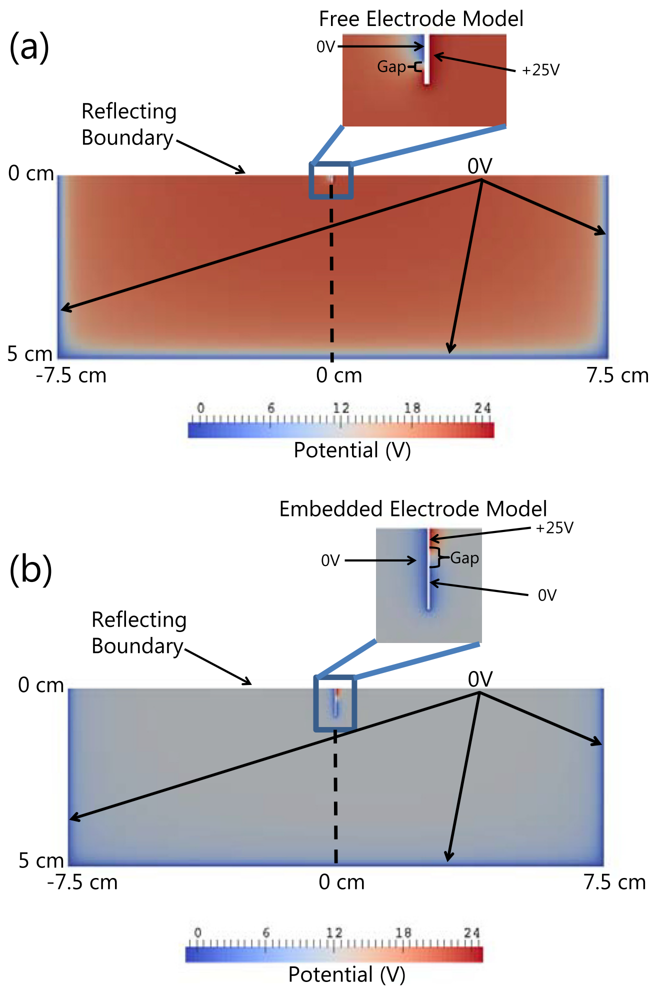

FIG. 2. PIC simulation domain, along with plasma potential, for each model electrode configuration: (a) free electrode model and (b) embedded electrode model.

velocity moment. The temperatures were computed from particle location and velocity data at 20 different time slices separated by 50 ns each, during the last 2 μs of the simulation. The resulting temperatures were 4.63 eV for the free electrode case and 2.43 eV for the embedded electrode, leading to ion sound speeds of 1.06×10^6 cm s^{-1} and 7.7×10^5 cm s^{-1}, respectively.

IV. RESULTS

A. Experiment results

1. Ion measurements

Axial and radial IVDF measurements are shown in Fig. 3 at several axial positions (note: axial and radial directions are in reference to the electrode symmetry axis, see Fig. 1). Data for each panel were taken separately with similar plasma conditions. Plasma parameters in the bulk were measured to be $n_e = 7.4 \times 10^9$ cm^{-3}, $T_e = 1.4$ eV, and $V_p = 5.0$ V when the free electrode was in place, and $n_e = 7.0 \times 10^9$ cm^{-3}, $T_e = 1.2$ eV, and $V_p = 4.1$ V when the embedded electrode was in place. The LIF signal from all PMT channels was summed to improve the signal to noise for this figure. Summing the channels removes the radial spatial resolution and slightly widens the distribution function (causing an apparent increase in ion temperature), but the random error bars were reduced to the approximate size of the plotted line width. Changes in the IVDFs as a function of axial position are most noticeable in the axial velocity component above the embedded electrode, where the ions accelerate to approximately half the sound speed toward the electrode surface (which is a negative velocity).

Axial IVDF measurements are shown in Figs. 4(a) and 4(b) at several radial positions. Panels (a) and (b) show data for the embedded and free electrodes, respectively, at axial position Z = 0.5 cm, which is where the most noticeable differences were observed between radial positions. These plots were made by summing the signal from the 16 radial channels into 4 equal sized bins, where each bin was 0.3 cm × 0.1 cm × 0.9 cm (width $\hat{r}$ × height $\hat{z}$ × depth). The curves were smoothed to reduce noise. The resulting random error bars are approximately the size of the plotted line width. Radial dependence of the flow moment was only observed for the embedded electrode, where non-Maxwellian flows increased with increasing radius. In the case of the free electrode, the flow was small, approximately Maxwellian, and did not show radial dependence.

Plots of ion flux near each electrode are shown in Figs. 5(a) and 5(b). Vectors represent ion flux, while contours show the observed plasma potential. The vector length is proportional to the product of the density and velocity moments which were calculated from the experimental IVDFs at each position. The LIF density measurements were referenced to the bulk plasma value found using the Langmuir probe. Vectors in all the panels have been scaled equally, with the longest arrow representing a flux of $n_i v_i = 3 \times 10^{20}$ cm^{-2} s^{-1}. Two separate density measurements were made at each position by integrating both axial and radial IVDF measurements individually. These were generally in good agreement ∼5%; however, a discrepancy of ∼30% was measured at certain locations near the embedded electrode and ∼10% near the free electrode. The cause of this discrepancy is suspected to be optical pumping,[22] where the metastable ion population is partially depleted at some location, causing a decrease in the LIF signal amplitude. No correction was applied to the data for this effect, the axial and radial density moments were simply averaged at each location. This was likely the largest source of error for the flux measurement, since the error in the velocity measurements was relatively small (3×10^3 cm s^{-1}). Although the error in the density measurement was relatively high, differences in the ion flux profile near each electrode are much more significant than this experimental uncertainty.

2. Potential

Measurements of the plasma potential are shown in Fig. 6. Data were taken in a 2D grid above each electrode with an emissive probe using the floating point method.[19] The random error for this measurement was approximately 50 mV due to small fluctuations in the plasma conditions over several minute time scales. Panels a and b show potential contours near the free and embedded electrodes, respectively. The potential step between contours was set equal for

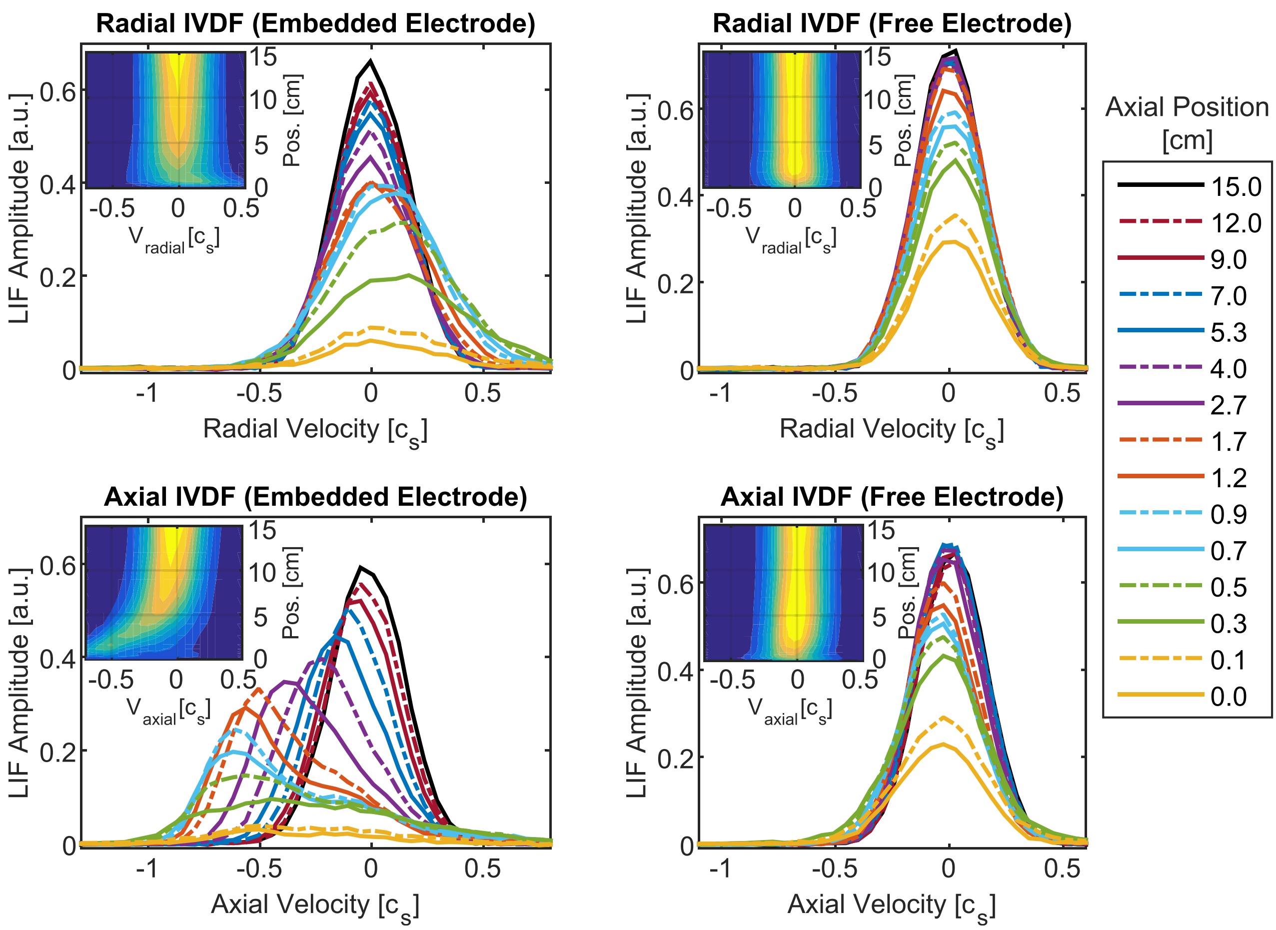

FIG. 3. Experimental IVDFs at different axial electrode positions are shown in different colors for each electrode and velocity component. Insert: contour version of the same data to show spatial changes more clearly.

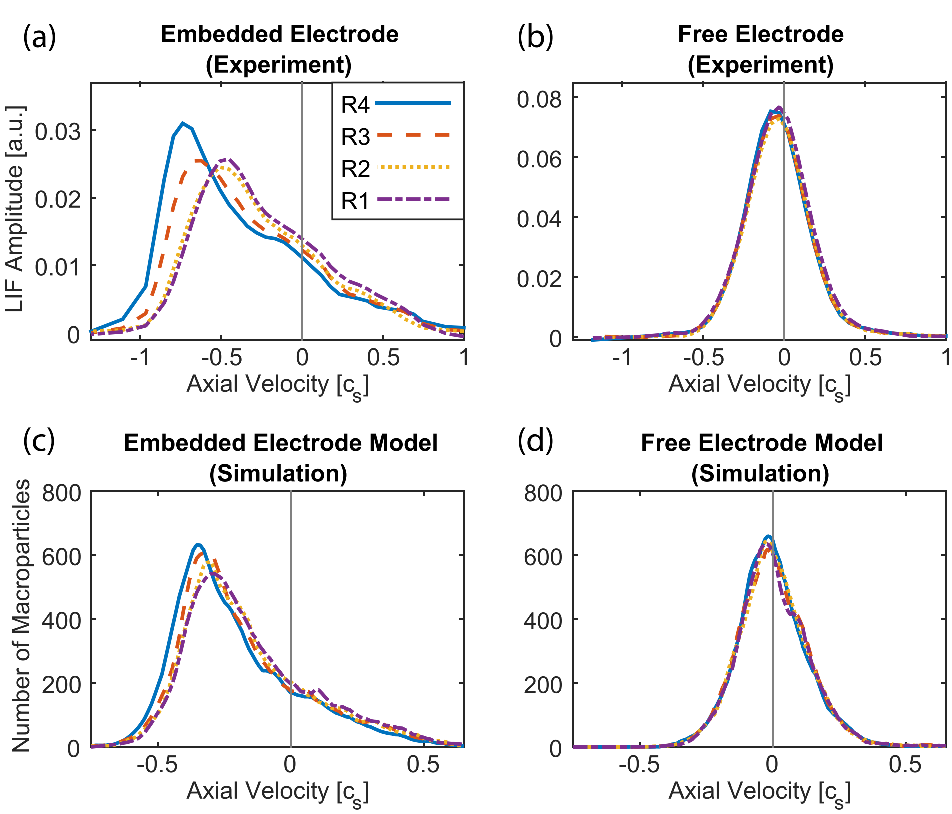

FIG. 4. Axial IVDF shown separated into 4 radial bins for each electrode at Z = 0.5 cm: ((a) and (b)) experimental data (bins centered at R1 = 0.0 cm, R2 = 0.3 cm, R3 = 0.6 cm, and R4 = 0.9 cm, where electrode radius = 0.95 cm), ((c) and (d)) simulation data (bins centered at R1 = 0.03 cm, R2 = 0.09 cm, R3 = 0.15 cm, and R4 = 0.21 cm, where electrode radius = 0.2 cm).

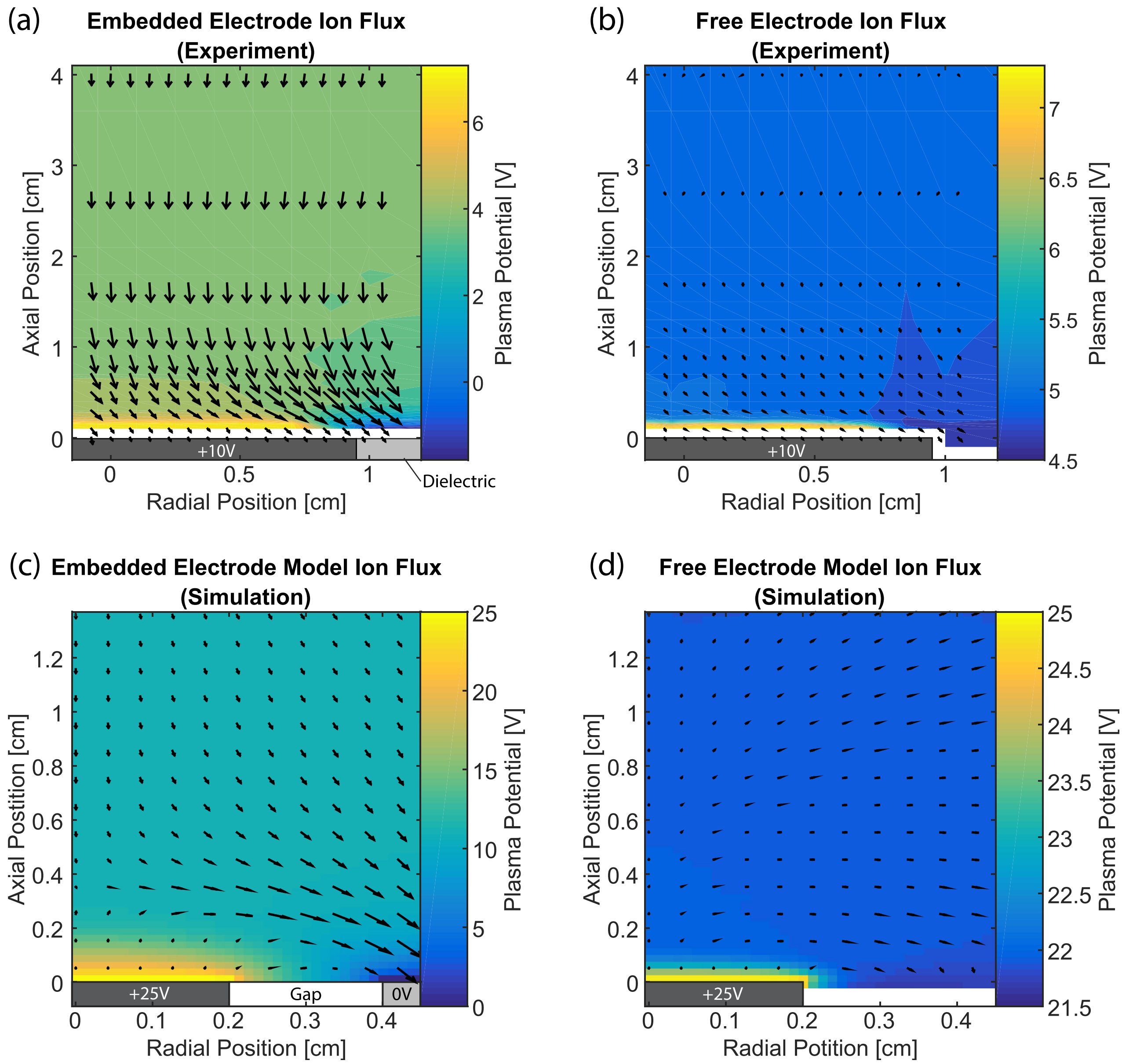

FIG. 5. Ion flux vectors shown with plasma potential in background: ((a) and (b)) from experimental data, ((c) and (d)) from simulation data averaged over last 100 000 time steps. Vectors in all panels have been scaled equally, with the longest arrow representing a flux of $n_i v_i = 3 \times 10^{20}\ \mathrm{cm^{-2}\,s^{-1}}$. Ion flux is much greater near the embedded electrode where ions flow toward and around the positively biased surface. The gap shown in the embedded electrode model (panel c) is a region where the surface potential was allowed to vary. This is a simulation requirement which prevents large fields from developing at the interface between biased regions.

both plots to emphasize the different potential gradient near the two electrodes. A virtual cathode can be seen above both electrodes although this dip is nearly at the noise level for the free electrode case. The 2D potential contours show that the virtual cathode near the embedded electrode is part of a saddle-shaped potential structure, similar to what was observed in Ref. 9. The shape of the virtual cathode can be seen more clearly in panel (c), which shows an axial profile near each electrode center. The virtual cathode is approximately 0.3 V deep above the embedded electrode compared to 0.1 V above the free electrode.

3. Discussion

The plasma potential and ion flow were observed to change significantly depending on the dielectric geometry. For the embedded electrode, the ion presheath appeared to encapsulate the electron sheath of the electrode (ion presheath length ∼5 cm, electron sheath length ∼0.1 cm). The resulting saddle-shaped potential structure formed a virtual cathode with the relatively large ion flow associated with an ion presheath and provided a mechanism for ion pumping. In the case of the free electrode, the dielectric was much smaller and located on the underside of the electrode. This reduced/eliminated the effect of the ion presheath above the electrode, where a very weak virtual cathode and ion flow were observed.

It was predicted in Ref. 11 that a small positive electrode would result in an approximately monotonic electron sheath, as we observed near the free electrode. However, a virtual cathode was observed near the embedded electrode despite being the same size. This virtual cathode appears to

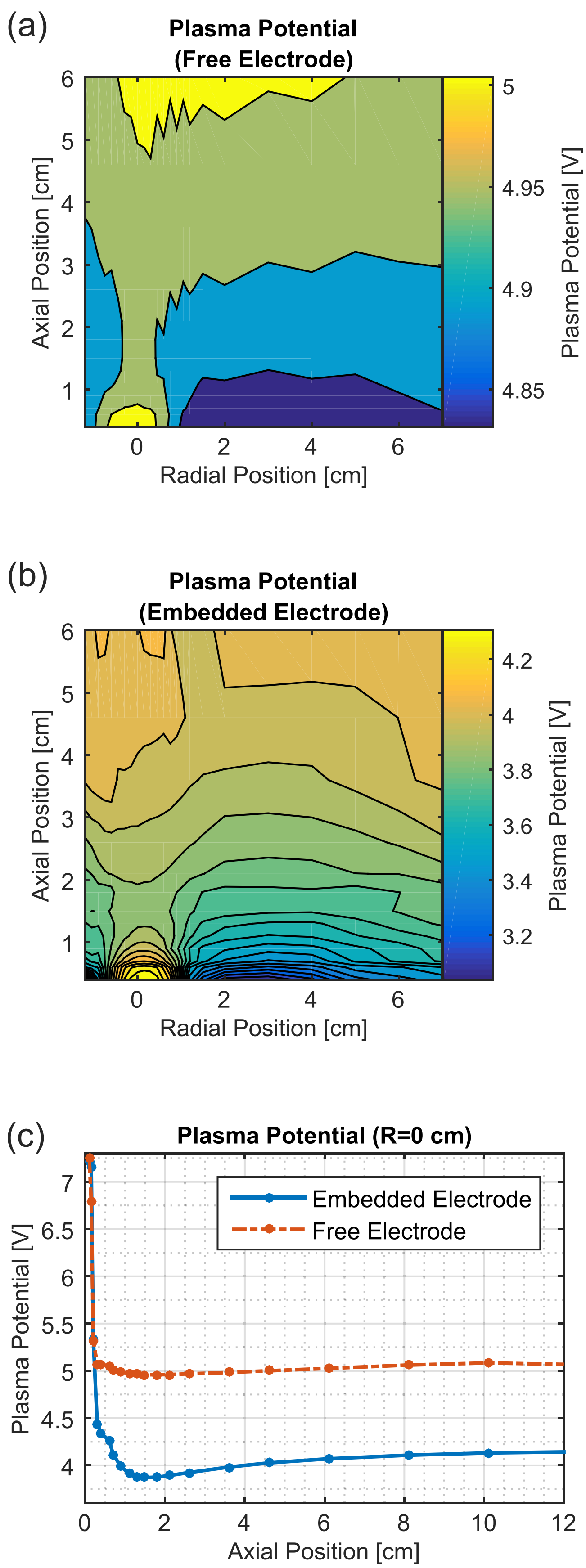

FIG. 6. Experimental measurements of plasma potential: (a) potential contour near the free electrode, (b) potential contour near the embedded electrode (c) slice of data near R = 0 for both electrodes. Data for axial positions less than Z = 0.4 cm are not shown in the contour plots so that smaller potential gradients are visible.

be caused by the far reaching ion presheath from the surrounding dielectric, which was not considered in Ref. 11. In this region, both ion presheath and electron presheath are present. Compared to ion presheaths, electron presheaths have a much smaller potential drop, are much longer in extent, and accelerate their particle (electrons) via a pressure gradient rather than electrostatically.[1] When the two presheaths interact, the electric field of the ion presheath dominates. The result is an axial potential profile which looks approximately like an ion presheath far from the electrode and an electron sheath near the electrode, as in Fig. 6(c).

Ion pumping of the virtual cathode appears to be accomplished geometrically. This is the same conclusion reached in Ref. 9. It appears that ions flowed out of the virtual cathode radially since they were only trapped in the axial direction. This is supported by potential measurements which show that the potential structure is saddle-shaped and by IVDF measurements which show ions flowing out radially from the potential dip. The saddle shape appears to be formed by the presheath associated with the dielectric expanding to overlap the region in front of the biased electrode.

B. Simulation results

IVDFs from the simulation are shown in Fig. 7 for each model electrode configuration. The figure shows 2D IVDF contour plots. These 2D profiles provide a detailed level of information that is not accessible from the 1D projections obtained from the LIF measurements, such as the boomerang-shaped structure in location 1E of the top panel. IVDF contours are shown at 20 spatial locations for each electrode geometry, with the binning area shown schematically to the right of each figure. As in the experimental measurements, the ions accelerated toward and around the embedded electrode, while comparatively little flow was observed near the free electrode.

IVDFs at different radial positions with axial velocity resolution are shown in Figs. 4(c) and 4(d). Both panels show data at axial position $Z = 0.5$ cm, which matches the location used in the corresponding experimental figure. This was done for convenience and because the IVDFs from the simulation become very noisy at smaller axial positions (due to low particle number). A better comparison would scale these locations based on relevant scale lengths, since the experiment and simulation were not identical. Each bin is $0.06\,\mathrm{cm} \times 0.06\,\mathrm{cm}$. The center of each bin was located at $r = 0.03$, 0.09, 0.15, and 0.21 cm, respectively (the electrode width is 0.2 cm). Although the flow velocities in the simulation were smaller than those measured experimentally, the simulation showed a good qualitative agreement. The smaller flow shift in panel (c) compared to (a) is likely due to the gap between the electrode and grounded surface in the simulation, which puts bin 4 much farther from the dielectric (really grounded conductor) surface than in the experiment. An exact agreement with the experiment was not expected, since: the simulation used helium rather than argon, the electrode geometry/materials were not identical, plasma conditions were not perfectly replicated, etc.

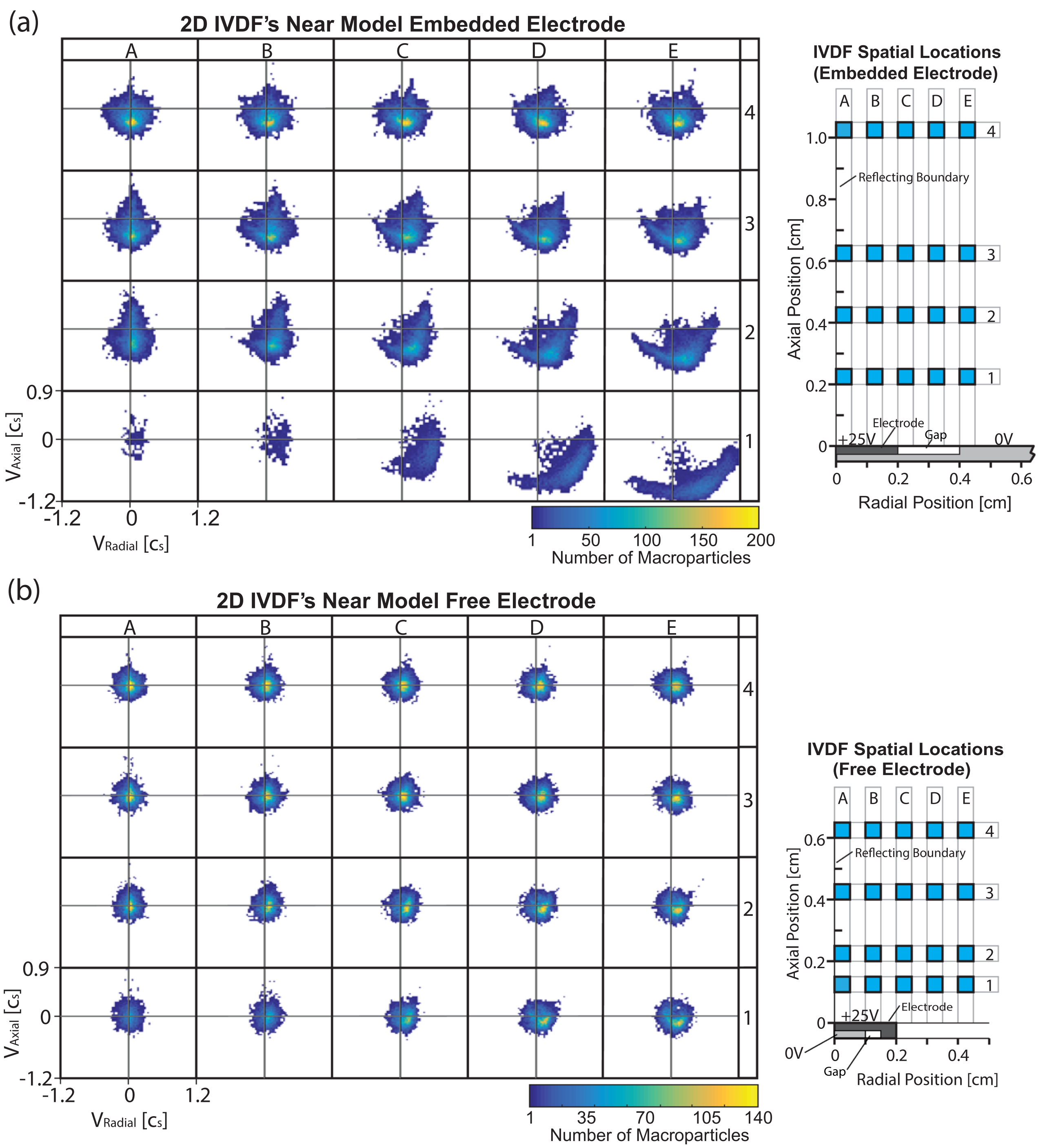

FIG. 7. 2D IVDFs from a PIC simulation of each model electrode geometry: (a) embedded electrode model and (b) free electrode model. Location and bin size for each measurement shown schematically on the right.

Plots of the ion flux near each model electrode are shown in Figs. 5(c) and 5(d). Vectors represent ion flux, while the plasma potential is shown in the background. Vectors in all panels were scaled equally, with the longest arrow representing a flux of $n_i v_i = 3 \times 10^{20}\,\mathrm{cm}^{-2}\,\mathrm{s}^{-1}$. Results approximately match those from the experiment, though the radial velocity is more pronounced in the simulation. This may be due to the relatively large 9 mm depth of field in the LIF measurements which will preferentially average out the radial velocity component. The salient features of the experiment are captured in the simulation: the axial flux is much higher for the embedded electrode, and the radial component is significantly larger in the region in front of the electron sheath for the embedded electrode.

Measurements of the plasma potential from the simulation are not presented (other than the backgrounds of Figs. 2 and 5) but were similar to the experimental measurements.

V. SUMMARY

Our measurements of plasma potential, ion flow, and ion density show that the geometry of a dielectric surrounding an electrode can produce features such as virtual cathodes and ion flows due to the ion presheath, which may surround the electron sheath. The case of the free electrode shows that isolating the surface of the electrode from dielectric insulation and minimizing the dielectric area can reduce these effects.

A qualitative agreement was seen between the experiment and simulation. In both cases, the ions flowed toward and around the embedded electrode with a significant fraction of the ion sound speed (nearly one half) and in both cases there was little flow induced near the free electrode. Although a quantitative agreement was not expected due to the differences between the two tests, an impressive agreement was observed.

These results may have implications for diagnostics and other applications where positively biased electrodes are used near dielectric surfaces. These include Langmuir probes, as well as control surfaces in fusion research devices[4,5] and electrodes used to control electron temperature in laboratory plasmas.[6] The virtual cathode and associated ion flow may alter the ion density profile and due to quasineutrality, the electron current to the boundary.

ACKNOWLEDGMENTS

This research was supported by the Office of Fusion Energy Sciences at the U.S. Department of Energy under Contract No. DE-AC04-94SL85000. In addition, B. Scheiner was supported by the Office of Science Graduate Student Research (SCGSR) program under Contract No. DE-AC05-06OR23100.

[1]B. T. Yee, B. Scheiner, S. D. Baalrud, E. V. Barnat, and M. M. Hopkins, "Electron Preheaths: The Outsized Influence of Positive Boundaries on Plasmas," Plasma Sources Sci. Tech. (to be published).
[2]F. F. Chen, *Plasma Diagnostic Techniques*, edited by R. H. Huddlestone and S. L. Leonard (Academic Press, New York, 1965), Chap. 4, p. 116.
[3]B. Scheiner, S. D. Baalrud, B. T. Yee, M. M. Hopkins, and E. V. Barnat, Phys. Plasmas **22**, 123520 (2015).
[4]S. J. Zweben, R. J. Maqueda, A. L. Roquemore, C. E. Bush, R. Kaita, R. J. Marsala, Y. Raitses, R. H. Cohen, and D. D. Ryutov, Plasma Phys. Controlled Fusion **51**, 105012 (2009).
[5]C. Theiler, I. Furno, J. Loizu, and A. Fasoli, Phys. Rev. Lett. **108**, 065005 (2012).
[6]C.-S. Yip, J. P. Sheehan, N. Hershkowitz, and G. Severn, Plasma Sources Sci. Technol. **22**, 065002 (2013).
[7]C.-S. Yip and N. Hershkowitz, J. Phys. D: Appl. Phys. **48**, 395201 (2015).
[8]S.-J. Oh, Y.-K. Lee, and C.-W. Chung, Phys. Plasmas **18**, 103511 (2011).
[9]C. Forest and N. Hershkowitz, J. Appl. Phys. **60**, 1295 (1986).
[10]H. Bailung, A. R. Pal, N. C. Adhikary, H. K. Gogoi, and J. Chutia, Plasma Sources Sci. Technol. **15**, 59 (2006).
[11]S. D. Baalrud, N. Hershkowitz, and B. Longmier, Phys. Plasmas **14**, 042109 (2007).
[12]K. M. Frederick-Frost and K. A. Lynch, Phys. Plasmas **14**, 123503 (2007).
[13]E. V. Barnat, G. R. Laity, and S. D. Baalrud, Phys. Plasmas **21**, 103512 (2014).
[14]J. Loizu, J. Dominski, P. Ricci, and C. Theiler, Phys. Plasmas **19**, 083507 (2012).
[15]B. Scheiner, S. D. Baalrud, M. M. Hopkins, B. T. Yee, and E. V. Barnat, Phys. Plasmas **23**, 083510 (2016).
[16]M. M. Hopkins, B. T. Yee, S. D. Baalrud, and E. V. Barnat, Phys. Plasmas **23**, 063519 (2016).
[17]M. D. Campanell and M. V. Umansky, Phys. Rev. Lett. **116**, 085003 (2016).
[18]I. A. Biloiu and E. E. Scime, Phys. Plasmas **17**, 113509 (2010).
[19]J. P. Sheehan, Y. Raitses, N. Hershkowitz, I. Kaganovich, and N. J. Fisch, Phys. Plasmas **18**, 073501 (2011).
[20]H. Timko, P. S. Crozier, M. M. Hopkins, K. Matyash, and R. Schneider, Contrib. Plasma Phys. **52**, 295 (2012).
[21]R. Courant, K. Friedrichs, and H. Lewy, Math. Ann. **100**, 32 (1928).
[22]G. D. Severn, D. A. Edrich, and R. McWilliams, Rev. Sci. Instrum. **69**, 10 (1998).